Linear stability analysis of salt fingers with surface evaporation or warming

Yuriko Yamamuro Renardy and Raymond W. Schmitt

Citation: Physics of Fluids (1994-present) **8**, 2855 (1996); doi: 10.1063/1.869067
View online: http://dx.doi.org/10.1063/1.869067
View Table of Contents: http://scitation.aip.org/content/aip/journal/pof2/8/11?ver=pdfcov
Published by the AIP Publishing

Linear stability analysis of salt fingers with surface evaporation or warming

Yuriko Yamamuro Renardy[a)]
Department of Mathematics, Virginia Polytechnic Institute and State University, Blacksburg, Virginia 24061-0123

Raymond W. Schmitt
Department of Physical Oceanography, Woods Hole Oceanographic Institution, Woods Hole, Massachusetts 02543

(Received 25 July 1995; accepted 31 July 1996)

Oceanic observations [Atmos. Ocean **29**, 340 (1991)] have revealed small-scale thermohaline plumes near the surface of a calm sea under warming conditions. The stratification was favorable for the double-diffusive salt finger instability, though a previously unreported up–down asymmetry was found in which narrow downward cells are balanced by a broader, weaker upwelling. The scales of the thermal structures are consistent with asymmetric hexagonal salt-finger modes [J. Phys. Oceanogr. **24**, 855 (1994)], but no selection mechanism for the asymmetry has previously been identified. This paper explores the influence of nonlinear profiles of temperature and salinity, as might arise due to surface evaporation or warming, on the linear stability problem in a salt-fingering regime. Three models are considered. In the first, a sharp, nonlinear solute-concentration gradient is applied at the upper boundary, as might arise by surface evaporation. A Bénard mode appears, driven by the destabilizing density gradient in the thin boundary layer and influencing motion only within the boundary-layer thickness. In the second model, a weak salinity gradient is introduced below the boundary layer; double-diffusive bulk modes influence the motion across the entire fluid. Nonlinear interaction of the boundary layer and bulk modes provides a mechanism for maintaining salt fingers with up–down asymmetry. The third model contains a large temperature gradient at the surface, as might arise from warming by solar radiation, overlying a quasi-isothermal region above a region of moderate gradient. The largest-growth modes are found to be salt fingers that extend throughout the middle region and disappear in the top and bottom regions. This vertical structure is close to that of the asymmetric salt fingers described in Osborn [Atmos. Ocean **29**, 340 (1991)]. The differing length scales of the regions impress an up–down asymmetry on plumes; this is expected to yield a hexagonal pattern at the onset. © *1996 American Institute of Physics.* [S1070-6631(96)02711-0]

I. INTRODUCTION

The subject of double diffusion covers the study of fluids in which there are gradients of two or more properties with different molecular diffusivities. In the ocean, heat and salt provide the competing properties and this subject is also known as thermohaline or thermosolutal convection.[1,2] Salt fingers are long narrow convecting cells that are set up when warm salty water lies above cold fresh water. Salt fingers are recognized as an important mechanism for oceanic mixing and salt transport in the main thermocline.[3–5] Recent observations by Osborn[6] suggest that the finger instability is important in near-surface waters as well. Of particular interest in his data was the finding of a distinct asymmetry in the fingers, which seemed to be best characterized as narrow, downward plumes surrounded by a broader, weaker upwelling. Schmitt[7] has found that the scales of Osborn's plumes are consistent with asymmetric solutions to the unbounded salt-finger problem, but provided no selection mechanism for the asymmetry. This paper examines two mechanisms which can be selected for asymmetric planforms, which are evaporation due to a dry atmosphere and warming due to solar radiation.

It is important to attempt to understand such phenomena, because the near-surface plumes identified by Osborn[6] must play a role in the structure of the diurnal warm layer observed under light wind conditions. The diurnal warm layer is often more than 0.5 °C and occasionally as high as 3.5 °C warmer than the water below.[8] This temperature gradient has direct consequences for near-surface sound propagation, the computation of air–sea fluxes (which usually use a cooler, bulk temperature), and the dynamical response of the ocean to the wind stress. As shown by Price *et al.*,[9] the near-surface stratification set up by diurnal heating can trap the momentum imparted by the wind stress to a shallow layer which they term the diurnal jet. The ''salt fountains'' seen by Osborn and modeled here would act to contribute to this stratification by downward transport of the (destabilizing) salt left behind by evaporation. A goal of future modeling and observational efforts should be to attempt to quantify the fluxes due to this phenomena. In this work, however, we are still trying to understand the most novel aspect of the observations, the asymmetric planform of the plumes.

The question of planform selection in salt fingers is typically addressed by beginning with a linear stability analysis of a basic solution which satisfies the governing equations, followed by analysis of solutions to the nonlinear amplitude equations close to the onset of instability. Many studies have

[a)]Corresponding author: Telephone: 540-231-8258, Fax: 540-231-5960, Electronic mail: renardyy@math.vt.edu

begun with a basic solution in which the solute concentration and the temperature are linear functions of the vertical variable z. An example is the work of Ref. 10, which shows that rolls are preferred over square cells for conditions modeling a salt-finger regime. In this paper, however, we focus on situations where additional mechanisms enter the formulation, causing the basic solution to depend nonlinearly on depth. In order to introduce a selection mechanism for the hexagonal pattern suggested by Schmitt[7] with descending warm parcels that are smaller and more intense than rising cool water, a nonlinear analysis is required. The techniques for weakly nonlinear analysis of bifurcating solutions at a finite critical wave number depend on whether the problem possesses midplane symmetry or not.[11,12] The motivation for developing models which do not have midplane symmetry is that *a priori* it would have a chance to generate planforms that are different from rolls. Two mechanisms that break the up–down symmetry will be addressed. The first is evaporation due to a dry atmosphere that occurs over several hours, leading to a salty layer at the top, with the salinity not varying much over the rest of the fluid [Figs. 1(a,b)]. The second is surface heating during a warm sunny day, leading to a nonlinear temperature profile [Fig. 1(c)]. The relevant values for the parameters of the models are discussed in Sec. II. Section III is a brief review of the classical double-diffusion problem, and together with Sec. II, this places the setting for the results in subsequent sections.

In Sec. IV, we develop a model which highlights the mechanism of surface evaporation for the instability leading to asymmetric salt fingers [Fig. 1(a)]. This seems appropriate as Osborn's[6] measurements (taken with a submarine near the ocean surface) show salt fingers extending down to 2–3 m. Data are not available near the surface in the first centimeter, but he notes that ''in the region very near to the surface, the trend toward saltier water at the surface is unmistakable.'' We assume that evaporation leads to a salty boundary layer of the order of a few millimeters, or perhaps centimeters. The basic temperature profile is the familiar linear function of z and provides a stabilizing environment. The surface salinity boundary layer is thin compared with the total length of the salt finger. Plumes that originate in the thin layer would be high-salinity plumes that sink and form the asymmetric structure.

The actual thickness of the salinity boundary layer would be determined by a number of surface effects such as the day/night cycle of temperatures and evaporation. We focus on a time interval of less than a day, examining a system that is changing slowly over that time, and modeling it as being in equilibrium over a time scale of minutes, during which the observations are made. The size of the finger spacing is deduced from the wavelength for the mode of largest growth. As a first step in attempting to understand the effect of evaporation, we apply linear theory in highly nonlinear regimes, and examine the modes of largest growth rates and corresponding wavelengths. It is inferred that the eigenfunctions may reflect the observed motions, which may be a reasonable assumption if they grow fast enough. Questions still remain regarding the observability, and there is need for controlled experiments.

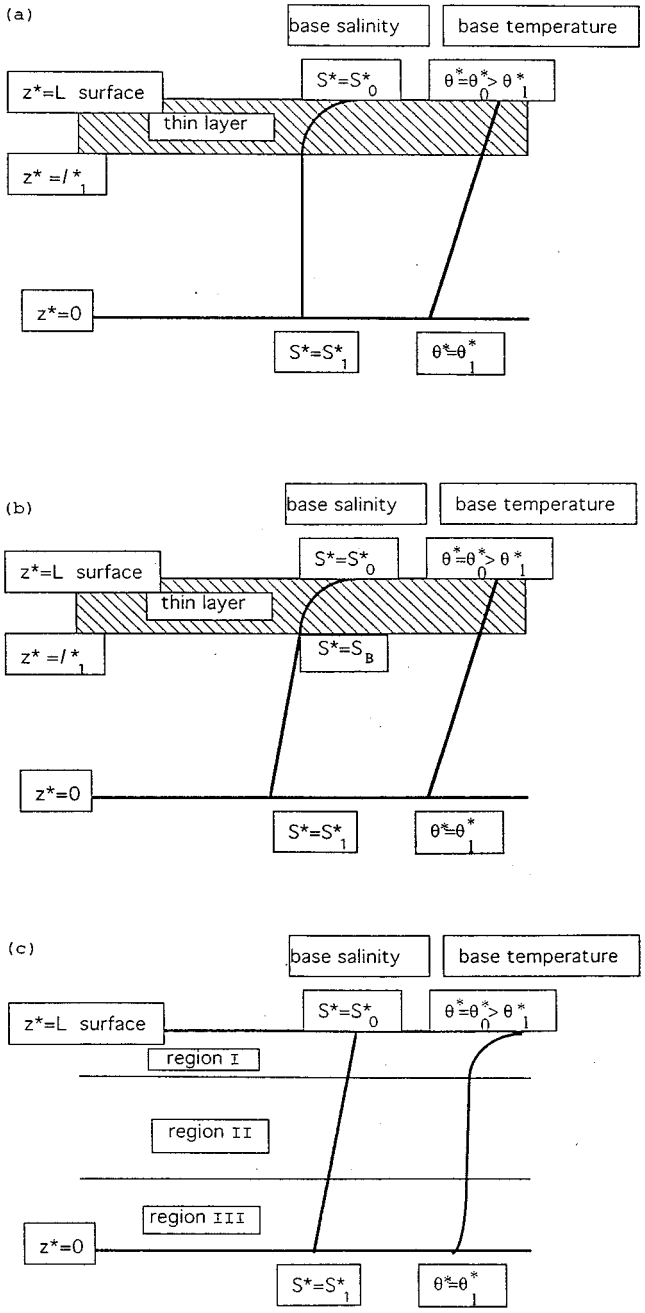

FIG. 1. A sketch showing profiles of base salinity and temperature for the three models we consider: (a) surface evaporation model with a thin salty boundary layer at the surface, (b) surface evaporation model modified with a mild salinity gradient in the bulk, (c) surface warming model.

In Sec. V, the salty boundary-layer model is modified by including a destabilizing salinity gradient in the bulk of the fluid, thus exciting bulk motion [Fig. 1(b)]. There are two families of modes which can become unstable: the boundary-layer modes and bulk modes. In contrast to the boundary-layer modes, the bulk modes are double diffusive, which arise from the competing diffusivities in the presence of a stabilizing density gradient. When these modes have comparable growth rates at the desired wave number, they would maintain asymmetric salt fingers. The evaporative boundary

layer, together with an interior salinity gradient, yields the possibility of asymmetric salt fingers. The motion in our model is driven both by the destabilizing density gradient in the boundary layer and the difference in diffusivities in the interior. However, the salty boundary-layer model is an unlikely explanation for the particular salt fingers observed by Osborn,[6] since he notes that they begin a half-meter down. Our model does not show any ability to trigger motions that begin that deep; it does not have an obvious mechanism for such a motion. It is therefore concluded that surface evaporation is not the main ingredient that leads to Osborn's asymmetric salt fingers.

The second mechanism which was investigated is a nonlinear temperature profile, which accounts for near-surface heating due to solar radiation [Fig. 1(c)]. Osborn describes his measured temperature field comprising three regimes. A top surface region 1 m thick has a strong gradient: below it is a quasi-isothermal layer 3 m thick, followed by a layer of steadily decreasing temperature. Salt fingers are observed in the middle layer. This motivates us to consider in Sec. VI a temperature profile that is steep in the first half-meter, then gradual for a few meters, then steeper below. In order to focus on the effect of this temperature profile, the salinity profile is taken as linear and evaporation is ignored. The salinity gradient is destabilizing, while the temperature gradients in the top and bottom layers are stabilizing. The competing mechanisms have the potential for setting up an instability in the middle layer, while stabilizing the top and bottom layers. The numerical results show that the largest growth rate modes consist of double-diffusive modes in the middle layer, with little action in the top and bottom layers. These replicate the vertical structure of plumes that begin at the bottom of the top layer, extend through the middle layer, and disappear into the top of the bottom layer. The up–down asymmetry in the modes for the surface warming model is a promising mechanism for driving nonlinear hexagonal patterns in the three-dimensional problem. The question of whether the hexagons can be excited nonlinearly close to onset will be addressed in future work.

II. CHOICE OF PARAMETERS

A fluid layer is bounded at $z^*=0, L$. The temperature and solute concentration at the upper boundary are θ_0^* and S_0^*, and the lower boundary is kept at temperature θ_1^* with solute concentration S_1^*. At temperature θ_0^*, the fluid has thermal coefficient of volume expansion $\hat{\alpha}$, solute coefficient of volume expansion $\hat{\beta}$, thermal diffusivity κ_T, solute diffusivity κ_S, viscosity μ, density ρ_0, and kinematic viscosity $\nu=\mu/\rho_0$. Dimensionless variables (without asterisks) are as follows: $(x,y,z)=(x^*,y^*,z^*)/L$, $t=\kappa_T t^*/L^2$, $\mathbf{v}=\mathbf{v}^*L/\kappa_T$, $\theta=(\theta^*-\theta_0^*)/(\theta_1^*-\theta_0^*)$, $S=(S^*-S_0^*)/(S_1^*-S_0^*)$, $p=p^*L^2/(\rho_0\kappa_2^T)$. A thermal Rayleigh number is defined by $R_T=g\hat{\alpha}(\theta_1^*-\theta_0^*)L^3/(\kappa_T\nu)$, where g denotes gravitational acceleration, a salinity Rayleigh number is $R_S=g\hat{\beta}(S_1^*-S_0^*)L^3/(\kappa_T\nu)$, a Prandtl number is $P=\nu/\kappa_T$, a Lewis number is $\tau=\kappa_S/\kappa_T$, and a dimensionless measure of gravity is $G=gL^3/\kappa_T^2$ (this appears only in the base pressure field in the subsequent analysis). There are four independent parameters: R_T, R_S, P, τ. Additional parameters in the salty boundary-layer model are the evaporation number c_E defined in Sec. IV and the salinity between the boundary layer and the bulk of the fluid s_B, defined in Sec. V. The nonlinear temperature profile model in Sec. VI introduces the thicknesses d_1, d_2 and temperatures θ_2, θ_3.

Because of the large number of parameters, we shall limit our presentation to oceanic values relevant to Osborn's[6] observations on asymmetric salt fingers. The thermal diffusivity $\kappa_T\approx 0.001$ (we use cgs units throughout); the salt diffusivity is $\kappa_s=10^{-5}$, $\rho=1$, and the kinematic viscosity $\nu\approx 0.01$ cm^2/s. The Prandtl number varies slightly with temperature. For the computations, we set $P=8$, $\tau=0.01$. The coefficient of thermal expansion $\hat{\alpha}$ for sea water is 2.2×10^{-4}/ °C.

We next estimate the parameter values relevant for the numerical results of Secs. IV and V. The temperature gradient for the bulk, extrapolated from Fig. 8 of Ref. 6 and Table 1 of Ref. 7, varies from 0.03 to 0.05 °C/m for the April 19 data, and from 0.08 to 0.36 °C/m for the data of April 24; thus, $(\theta_0^*-\theta_1^*)/L$ varies over 0.03–0.36 °C/m. The vertical length L of the salt finger is 2–3 m. With $g=980$ in cgs units, the thermal Rayleigh number varies from $R_T=-6\times10^{11}$ to -10^{10}. We denote $R_\rho=R_T/R_S$ and Table 1 of Ref. 7 gives R_ρ varying between 10 and 20. The thickness of the salty boundary-layer l_2^* may be on the order of millimeters, or even centimeters. As a situation to investigate numerically, we may take $(\theta_0^*-\theta_1^*)/L=0.1$ °C/m, $L=2$ m, yielding $R_T=-2.9\times10^{10}$. The solute coefficient of volume expansion $\hat{\beta}=0.8$ units per concentration, so that $R_\rho=11.7$, $R_S=-2.5\times10^9$. The observed salt fingers of Ref. 6 are approximately 4–8 cm in diameter, with cell spacing varying from 9 to 20 cm.

III. THE FAMILIAR MODEL OF DOUBLE DIFFUSION

In the classical double-diffusion problem (cf. Chap. 8 of Ref. 1), the following are the transport equations for the temperature and solute concentration, the Navier–Stokes equation with the Oberbeck–Boussinesq approximation and incompressibility: $\dot{\theta}+(\mathbf{v}\cdot\boldsymbol{\nabla})\theta=\Delta\theta$, $\dot{S}+(\mathbf{v}\cdot\boldsymbol{\nabla})S=\tau\Delta S$, $\dot{\mathbf{v}}+(\mathbf{v}\cdot\boldsymbol{\nabla})\mathbf{v}=P\Delta\mathbf{v}-\boldsymbol{\nabla}p+(R_TP\theta-R_SPS-G)\mathbf{e}_z$, $\mathrm{div}\,\mathbf{v}=0$. Salinity and temperature are prescribed at the plates: $\theta=1$ and $S=1$ at the bottom $z=0$, $\theta=0$ and $S=0$ at the ocean surface $z=1$. The velocity boundary condition is no slip: $\mathbf{v}=\mathbf{0}$ at $z=0,1$. (A more appropriate condition for the ocean surface may be the ''stress-free'' boundary condition, for which the eigenfunction is available in closed form.[1,13–16] In this case, the velocity boundary condition is zero normal velocity and zero shear stress.) A solution is $\mathbf{v}=\mathbf{0}$, $\theta=1-z$, $S=1-z$, $p=p_0-Gz+(R_T-R_S)P(z-z^2/2)$, where p_0 is a constant. The stability of this solution has been examined extensively in the literature. For the no-slip condition, criticality for the convective onset[1,17,18] is given by $R_T-R_s/\tau=1707.765$, $\alpha=3.12$, where α is the dimensionless horizontal wave number. For the stress-free condition, criticality is given by $R_T-R_s/\tau=27\pi^4/4$, $\alpha=\pi/\sqrt{2}$. The oceanic values discussed in Sec. II for both the no-slip and stress-free conditions are far above criticality with many modes un-

stable over a large interval of wave numbers. At such high Rayleigh numbers, we may neglect the effect of the boundaries except in boundary layers and, for the bulk of the flow, apply the time-dependent depth-independent similarity solution of Ref. 19. The motion is purely vertical and the governing equations linear. There are an infinite number of such solutions, with no *a priori* selection mechanism to favor any particular one, and they can be superposed. The vertical velocity is $w=\hat{w}\exp(\sigma t)\phi(x,y)$ where ϕ is a spatial planform function that satisfies the Helmholtz equation. A rough estimate for the growth rate σ and horizontal wave number α for maximum growth are

$$\sigma=O(|R_T|^{1/2}),\quad \alpha=O(|R_T|^{1/4}). \tag{1}$$

Exact values are given in Figs. 1–4 of Ref. 19. In this linear theory, there are an infinite variety of planforms, as long as the total horizontal wave number equals α. This wave number is the one obtained from a two-dimensional linear stability analysis. There is no selection mechanism for the linear theory. In order to explore planforms that correlate with Osborn's observations of asymmetric salt fountains, Schmitt[7] compared the cell spacing of triangular and hexagonal planforms. He found that the hexagonal planform with $\phi(x,y)=0.5\cos(\alpha y)+\sin(\sqrt{3}\alpha x/2)\sin(\alpha y/2)$ compares favorably. In this planform, the descending warm parcels are narrower and more intense than rising cool water, unlike the familiar sinusoidal salt-finger solutions. His Table 1 shows a prediction of the cell size of 2–4 cm and spacing ''Q'' of 5–10 cm. For his model, the cell spacing Q is the wavelength of largest growth rate in the linear stability analysis.

The question remains as to why the hexagonal pattern would be preferred over the others. One explanation is to consider weakly nonlinear effects. In the classical double-diffusion (or the simpler Bénard) problem, if the problem has up–down symmetry, the roll solution is preferred over hexagons.[10,11,20,21] When the up–down symmetry is broken, then the observed solution is the subcritical hexagon.[22] This provides the motivation in this paper for examining additional effects which introduce the up–down asymmetry. The linear stability results will be followed up in a subsequent paper concerning preferred patterns. The group theoretic results of Ref. 12 may be applied to find families of solutions that include the triangular and hexagonal types.

IV. AN EVAPORATIVE BOUNDARY-LAYER MODEL

A. Formulation of equations

The linear salinity and temperature profiles considered in the previous section are equilibrium solutions of the diffusion equation. In reality, however, temperature and salinity of the ocean are influenced by a number of factors which fluctuate with time, and equilibrium is never achieved. Diffusion is a slow process and, even profiles which are not steady-state solutions will not change appreciably over a period of hours if they are used as an initial condition. We shall assume the profiles are stationary and do a linear stability analysis around them (if the time scale for the growth of the instability is short relative to the time scale over which the base profile is varying, such an assumption is justified. The situation is analogous to the familiar case of boundary layer profiles in shear flows, which also do not really exist as steady solutions of the Navier–Stokes equations).

In a later section, we shall consider a nonlinear temperature profile, which takes account of solar heating near the surface and represents a qualitative fit to measurements. The variation of the temperature there occurs over the scale of roughly 1 m. The diffusivity for salinity is even smaller than that for heat, so we can think of profiles as quasisteady even if they vary over length scales less than 1 cm. Specifically, we are now interested in studying salinity profiles which contain a thin, salinity-enriched layer near the surface [Fig. 1(a)] arising from surface evaporation during the day. The surface evaporation condition is[23]

$$\kappa_s\partial S^*/\partial z^*=ES^*/\rho, \tag{2}$$

where E/ρ is the evaporation rate. Here, the small evaporation rate is balanced by small diffusivity. This is a boundary condition for the diffusion equation $\partial S^*/\partial t^*=\kappa_s\Delta S^*$. To show how a salt-enriched layer develops when evaporation is increased, let us consider for simplicity the case of an initially uniform salinity S_0^*, with no evaporation. Evaporation begins at time $t^*=0$. We now set $S^*=S_0^*+\tilde{s}$, and subsequently the deviation $\tilde{s}$ from uniform salinity is given by $\tilde{s}(\sqrt{\kappa_s t^*}\xi,t^*)=\sqrt{t^*}\phi(\xi,t^*)$, where the boundary-layer variable is $\xi=(z^*-L)/\sqrt{\kappa_s t^*}$. At the top surface, $\xi=0$. By inserting these relations into the diffusion equation and boundary conditions, we find

$$t^*\phi_t=\phi_{\xi\xi}+\frac{\xi}{2}\phi_\xi-\frac{1}{2}\phi,\quad t^*>0,\quad \xi<0 \tag{3}$$

with boundary condition $\sqrt{\kappa_s}\phi_\xi=(E/\rho)S_0^*+(E/\rho)\sqrt{t^*}\phi$ at $\xi=0$. For small t^*, we neglect the terms which contain factors t^* and $\sqrt{t^*}$. Equation (3) together with the condition $\phi\to 0$ as $\xi\to-\infty$ leads to a solution ϕ which is a multiple of a function of only ξ. The constant of multiplication is uniquely characterized by the boundary condition at $\xi=0$. Thus, the magnitude of the solution ϕ is proportional to $ES_0^*/(\rho\sqrt{\kappa_s})$. In terms of the original variables, therefore, the thickness of the salinity-enriched layer is of order $\sqrt{\kappa_s t^*}$ and the salinity excess at the surface is of order $ES_0^*\sqrt{t^*}/(\rho\sqrt{\kappa_s})$. We can use this to obtain some estimates. In cgs units, κ_s is about 10^{-5}, and a reasonable value of t^* is of order 10^4. Hence, the boundary-layer thickness would be of order 10^{-1} to 1. The evaporation constant E/ρ is estimated to be of order 10^{-6}, and hence the salinity increase in the boundary layer would be about one order of magnitude less than S_0^*. In the calculations below, we assume a boundary-layer thickness l_2^* of 2.5 mm, and an evaporation constant of 10^{-6} cm/s. The salinity outside of the boundary layer is approximated by $S_1^*=35\times 10^{-3}$. We may use Eq. (2) and the particular value of l_2^* to estimate that the decrease in salinity across the boundary layer is 0.0008. Effects of changing l_2^* are discussed below in Sec. IV D.

In our model, we do not actually solve the diffusion equation to obtain a boundary-layer profile because the assumptions above are grossly simplified anyway (for example, E is not constant), and, qualitatively, we expect that

the detailed structure of the profile is not crucial. Hence, we shall choose a profile which captures the main qualitative features and is simple to use. This salinity profile has a linear variation over most of the flow region, except in a thin layer at the top. In this thin layer, we assume a polynomial dependence on z as evident below.

In dimensionless variables, we have the boundary conditions $\theta=0$ at $z=1$ (top surface), $\theta=1$ at $z=0$ (bottom), and we have a base state with zero velocity and linear temperature: $\mathbf{v}=\mathbf{0}$, $\theta=1-z$. For the salinity, the dimensionless form of the condition at the top surface is

$$\frac{\partial S}{\partial z}=a_E+\frac{c_E S}{l_2},\quad l_2=\frac{l_2^*}{L},\quad c_E=\frac{l_2^* E}{\rho\kappa_s},\quad a_E=-(1+c_E)/l_2. \tag{4}$$

Here l_2^* denotes the thickness of the boundary layer. For the parameters quoted above, c_E is approximately 0.023. We start by analyzing a base profile where the salinity is constant outside the boundary layer, and increases sharply close to the ocean surface:

$$S=\begin{cases}1 & \text{for } 0<z_1<l_1\\ 1+c_n(z-l_1)^n & \text{for } l_1<z<1,\end{cases} \tag{5}$$

where $1-l_2=l_1$, and $n=2, 3,...$, so that the salinity and salinity flux are continuous at $z=l_1$. To satisfy the top surface condition (4), $c_n=-1/[l_2^n(n-c_E)]$. The basic pressure p is

$$p=\begin{cases} p_0-Gz+R_TP\left(z-\dfrac{z^2}{2}\right)-R_SPz & \text{outside the boundary layer}\\ p_0-Gz+R_TP\left(z-\dfrac{z^2}{2}\right)-R_SP(z+c_n(z-l_1)^{n+1}/(n+1)) & \text{in the boundary layer,}\end{cases} \tag{6}$$

where p_0 is a constant. This basic pressure field is a response to the system, and does not enter into the linear stability analysis.

The difference between (θ,S,p) and the basic solution $\mathbf{v}=\mathbf{0}$, $\theta=1-z$, (5), (6), is denoted by $(\tilde\theta,\tilde S,\tilde p)$. The equations for $0\leqslant z\leqslant l_1$ are

$$\dot{\tilde\theta}-w-\Delta\tilde\theta=-(\mathbf{v}\cdot\boldsymbol{\nabla})\tilde\theta, \tag{7}$$

$$\dot{\tilde S}-\tau\Delta\tilde S=-(\mathbf{v}\cdot\boldsymbol{\nabla})\tilde S, \tag{8}$$

the momentum equation, $\dot{\mathbf{v}}-P\Delta\mathbf{v}+\nabla\tilde p+(R_SP\tilde S-R_TP\tilde\theta)\mathbf{e}_z=-(\mathbf{v}\cdot\boldsymbol{\nabla})\mathbf{v}$, and incompressibility $\operatorname{div}\mathbf{v}=0$. The equations for $l_1\leqslant z\leqslant 1$ are the same except that (8) is changed to

$$\dot{\tilde S}+w\frac{\partial S}{\partial z}-\tau\Delta\tilde S=-(\mathbf{v}\cdot\boldsymbol{\nabla})\tilde S, \tag{9}$$

where S is the boundary layer solution (5). The boundary conditions are $\tilde\theta=0$ at $z=0,1$,

$$\frac{\partial\tilde S}{\partial z}=\frac{c_E\tilde S}{l_2}\quad\text{at the top } z=1, \tag{10}$$

$$\tilde S=0\quad\text{at the bottom } z=0, \tag{11}$$

$\mathbf{v}=0$ at $z=0,1$. The conditions at $z=l_1$ are the following; $[\![f]\!]$ denotes $f(z=l_1^-)-f(z=l_1^+)$. Continuity of velocity yields $[\![\mathbf{v}]\!]=0$. Since w is continuous, $[\![\partial w/\partial y]\!]=\partial[\![w]\!]/\partial y=0$, and $[\![\partial w/\partial x]\!]=\partial[\![w]\!]/\partial x=0$. Hence, balance of shear stresses yields $[\![\partial u/\partial z]\!]=0$, $[\![\partial v/\partial z]\!]=0$. By incompressibility, $\partial w/\partial z=-\partial u/\partial x-\partial v/\partial y$. Therefore, $\partial w/\partial z$ is continuous at $z=l_1$. Hence, the normal stress balance yields continuity of pressure perturbation: $[\![\tilde p]\!]=0$. Continuity of temperature, heat flux, salinity and salinity flux yield, respectively, $[\![\tilde\theta]\!]=0$, $[\![\partial\tilde\theta/\partial z]\!]=0$, $[\![\tilde S]\!]=0$, $[\![\partial\tilde S/\partial z]\!]=0$.

B. Linearized stability analysis

Due to the symmetries in this problem, the linear stability analysis can be done in the $x-z$ plane, ignoring the y dependence. We seek normal mode solutions proportional to $\exp(i\alpha x+\sigma t)$. This leads to an eigenvalue problem for σ. The Chebyshev-tau method,[24–27] is used to discretize the governing equations with respect to the z variable. This method approximates the eigenvalues for C^∞ eigenfunctions with infinite-order accuracy. Since much of the action will be found to take place in the very thin boundary layer, we will need to use many more Chebyshev modes in the lower layer to match up to the dynamics in the upper layer. We discretize $\tilde\theta$, $\tilde S$, and w using Chebyshev polynomials of degree 0 to $M\times N$ in the lower layer and N in the upper layer; for example,

$$\tilde\theta=\exp(i\alpha x+\sigma t)\times\begin{cases}\displaystyle\sum_{n=0}^{N\times M} t_{1n}T_n(z_1) & \text{in the lower layer}\\ \displaystyle\sum_{n=0}^{N} t_{2n}T_n(z_2) & \text{in the boundary layer,}\end{cases} \tag{12}$$

$$z_i=\begin{cases}(2/l_1)z-1, & \text{(lower layer) } 0<z<;_1\\ (2/l_2)z+1-(2/l_2) & \text{(upper layer } l_1<z<1,\end{cases}$$

$-1<z_i<1$. This results in $3(MN+1)$ unknown coefficients in the lower layer and $3(N+1)$ unknown coefficients in the upper layer, a total of $3MN+3N+6$ unknowns. The appropriate values for M and N are found through convergence tests on the computed eigenvalues.

We use incompressibility to eliminate u in favor of w, and use the x component of the momentum equation to eliminate p. This reduces the momentum equation

to $\sigma(\alpha^2 w - w_{zz}) + P(w_{zzzz} - 2\alpha^2 w_{zz} + \alpha^4 w) + \alpha^2(R_S P\tilde{S} - R_T P\tilde{\theta}) = 0$. This equation is discretized and truncated at the $(MN-4)$th Chebyshev mode in the lower layer and at the $(N-4)$th Chebyshev mode in the boundary layer, since the highest derivative appearing in the equation is the fourth derivative, and this indicates that the truncated system would be accurate to at most the $(MN-4)$th and $(N-4)$th degrees, respectively. The linearized forms of the solute transport equations (8), (9) are truncated beyond the $(MN-2)$th degree in the lower layer and $(N-2)$th degree in the boundary layer, as are the heat transport equations (7) in both layers. This results in $3MN+3N-10$ equations. The conditions at $z=l_1$ for the velocities and stresses reduce to the continuity of w, w_z, w_{zz}, and w_{zzz}. At the boundaries $z=0,1$, the velocity conditions are that $w=0$ and w_z vanish. Altogether, there are 16 boundary and $z=l_1$ conditions. This results in a $3MN+3N+6$ matrix eigenvalue problem.

C. The long-wave limit

In the limit of long-wave perturbations ($\alpha=0$), the linearized stability analysis is independent of the Rayleigh numbers. The vertical component of the velocity w satisfies $-\sigma w_{zz} + P w_{zzzz} = 0$, with $w=0$ at the top and bottom boundaries, and w, w_z, w_{zz}, w_{zzz} continuous at $z=l_1$. Therefore, the solution is $w=0$ in both layers. The problem for the solute concentration consists of Eqs. (8)–(11), and when $\alpha=0$, $w=0$, these become a Sturm–Liouville system: $\tilde{S}_{zz} - (\sigma/\tau)\tilde{S} = 0$, $\tilde{S}_z(1) = (c_E/l_2)\tilde{S}(1)$, $\tilde{S}(0)=0$. Hence, the eigenvalues σ are real, discrete and there are an infinite number of them. To find them, we consider three cases: $\sigma>0$, $\sigma=0$, and $\sigma<0$. For $\sigma>0$, the solution is $\tilde{S} = \sqrt{(\sigma/\tau)} \times \cosh\sqrt{(\sigma/\tau)}z$, where $\sqrt{(\sigma/\tau)}(l_2/c_E) = \tanh(\sqrt{\sigma/\tau})$. There is one root, and we can estimate it for the oceanic values. When τ is small, and σ is order one, $\sqrt{\sigma/\tau}$ is large enough that the hyperbolic tangent function is approximately 1. Thus,

$$\sigma \approx \left(\frac{c_E}{l_2}\right)\tau. \tag{13}$$

This is positive, giving an unstable long-wave mode. For the case $\sigma=0$, there is no eigenfunction. For the case $\sigma<0$, the eigenfunctions are $\tilde{S} = \sin(\sqrt{-\sigma/\tau})z$ where

$$x \Big/ \left(\frac{c_E}{l_2}\right) = \tan x, \quad x = \sqrt{\frac{-\sigma}{\tau}}. \tag{14}$$

We can estimate the eigenvalues closest to 0 as follows: since c_E/l_2 is large, the slope of the line represented by the left-hand side of (14) is close to flat, so it would intersect the tangent function close to where it hits 0, that is, at multiples of π plus a small positive quantity $\sigma \approx -(n^2\pi^2+\epsilon)\tau$, $0<\epsilon$, $n=1,2,...$. Our computer code was checked at $\alpha=0$.

The unstable long-wave mode irrespective of the Rayleigh numbers is one which is not present in the classical double-diffusion problem. This feature implies that there is no neutrally stable situation, or ''onset'' condition, in this model. Since we seek modes which grow to visible effect on the order of hours, it is more appropriate to examine largest growth-rate modes.

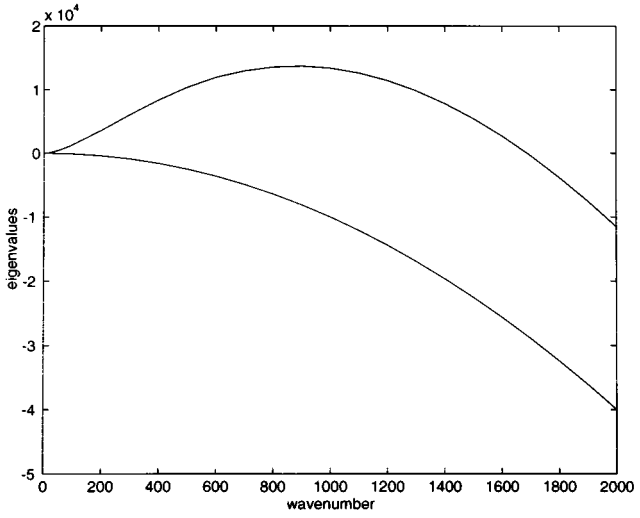

FIG. 2. Graph of the leading eigenvalues σ, the unstable mode, and the first of the stable mode, vs wave numbers α for $R_T=-2.9\times10^{10}$, $R_S=-2.5\times10^9$, $l_1=0.998\,75$, $c_E=0.022\,85$, $\tau=0.01$, $P=8$.

D. Numerical results

Numerical results show that the motion is confined to the upper boundary layer with little going on below; the length scale of variation is the thickness of that boundary layer. Since this is relatively small, if N Chebyshev modes suffice to describe what is going on in the boundary layer, then many more modes are used to properly match that motion in the lower layer. Our results have been tested for convergence. The following numerical results concern the case $n=2$ in the salinity profile (5). We focus on the oceanic parameters of Sec. II and examine modes of largest growth rates, to illustrate the motion that might be observed during morning hours, that would be set up in at most several hours.

The first case we consider is $P=8$, $\tau=0.01$, $R_T=-2.9\times10^{10}$, $R_S=-2.5\times10^9$, $l_1\approx0.999$ for a boundary layer thickness of 2.5 mm ($c_E=0.023$). The eigenvalues for wave numbers over the range 0–2000 were examined. A single mode is found to be unstable over a wide range; there is stability for wave numbers beyond 1700. The unstable mode is analogous to the single unstable root of (13) that is described in Sec. IV C for the case of long-wave disturbances. Figure 2 shows the growth rate $\mathrm{Re}\,\sigma$ against the wave number α, showing that the peak occurs around $\alpha=900$, where $\sigma=13702$ ($M=4$, $N=40$ in the notation of Sec. IV B). Figure 2 also shows the first of the stable modes over the same range of wave numbers; there are infinitely many more stable modes. These modes follow on the roots of (14). The magnitude of the peak growth rate is roughly of the same order as the depth-independent similarity solutions of Ref. 19: applying Eq. (1), we estimate a peak at α of $O(400)$ and growth rate of order 10^5. We shall call the modes the *boundary layer modes*. These are Benard-type modes, driven by the destabilizing density gradient in the thin boundary layer, and influences the motion on the length scale of the boundary layer thickness. If the boundary layer were thicker, for instance, more than one mode may be unstable.

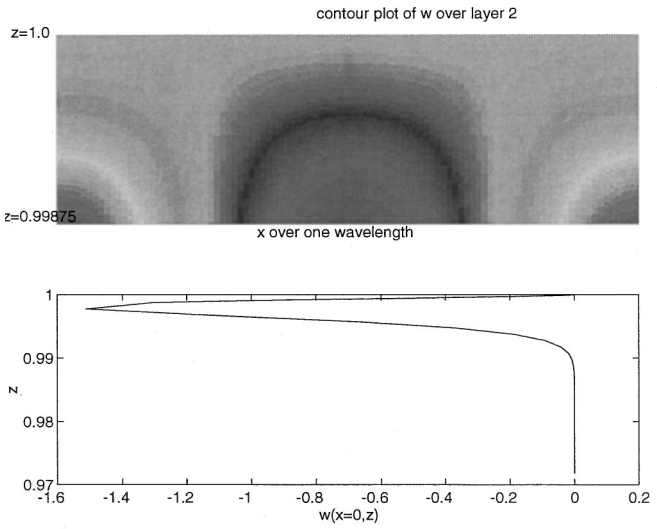

FIG. 3. Upper: contour plot of the vertical component of the velocity $w(x,z)$ for the boundary layer; the vertical axis is $z, l_1 \leqslant z \leqslant 1$, the horizontal axis is x extending over one wavelength $0 \leqslant x \leqslant 2\pi/\alpha, \alpha = 900$; this is the unstable mode at the parameters of Fig. 2. Lower: $w(x=0,z)$ vs z, $0.97 < z < 1$, at $x=0$, contour values for the upper figure can be obtained from the lower.

These are distinguished from *bulk modes* which will be discussed in Sec. V.

To relate the results to dimensional scales, recall that the dimensional wavelength is $\lambda^* = 2\pi L/\alpha$ cm, and for $L=200$ cm, $\alpha=900$ corresponds to $\lambda^*=1.4$ cm, which is short compared with the Osborn data discussed in Sec. II. Our normal mode is proportional to $\exp(\sigma \kappa_T / L^2 t^*)$, where t^* is the dimensional time, so that the mode will grow by a factor e after time $t^* = L^2/(\kappa_T \sigma)$. For our parameters, $\kappa_T / L^2 = 0.25 \times 10^{-7}$ s^{-1}. Thus, the unstable mode at $\alpha=900$ grows by a factor e in 50 min. Compared with this, the mode at $\alpha=20$ with $\sigma = O(100)$ takes about 100 h. When the time scale is this long, then other effects must be taken into consideration, such as the day/night cycle of evaporation and temperature changes, and shears and mixing associated with waves and wind stress. The observations were made during the late morning hours.

Since the lower layer has no salinity gradient and the temperature gradient is stabilizing, we expect little to be going on in the lower layer. The eigenfunction at $\alpha=900$ reflects this expectation to a large degree. Figure 3 shows the variation of the vertical component of the perturbation velocity w vs z. The upper plot is a contour plot over the boundary layer, and the lower plot shows w along $x=0$ over the larger region $0.97 \leqslant z \leqslant 1$. The contour values for the upper plot can be found from the lower plot; the x variation is simply sinusoidal. Note that the upper plot is zoomed into the top layer where the first peak in the lower plot occurs. The velocity hits its maximum magnitude at about $z = l_1$; at $z=0.99$, w is already 1% of the maximum magnitude. Figure 3 shows up–down asymmetry in the velocity profile about the position $z = l_1$, with a more gradual decline in the lower layer. The velocity is confined to a few boundary layer depths, below which there is relatively little motion. Table I shows the first five coefficients of the Chebyshev expansion, showing that the magnitudes in the lower layer are a fraction of those of the upper layer. Thus, the destabilizing salinity profile in the boundary layer drives a motion which is effectively damped out in the lower layer.

The effect of changing the Rayleigh numbers was examined. As the Rayleigh numbers are decreased, both the maximum growth rate and the wave number for the maximum growth rate decrease. This is similar to the effect of lowering the Rayleigh numbers in the depth-independent problem of Eq. (1).

The effect of increasing the boundary layer thickness is that the effective Rayleigh number increases for that region, and thus more modes are destabilized. When the thickness is increased tenfold, several modes are unstable and their growth rates are larger (Fig. 4). The wave number for the largest growth rate decreases because the motion is driven by the salinity profile in the boundary layer, and therefore, if the boundary-layer thickness is increased, the relevant length scale becomes larger. The growth rates are much higher because the effective Rayleigh numbers are those that are defined on the boundary-layer thickness, and these increase when that thickness increases. The unstable modes have eigenfunctions that describe convective rolls confined to a depth of two boundary layers or so, and is negligible below. The first mode has a one-cell structure, the second largest growth rate mode has a two-cell structure, and so on. It is evident that these boundary layer modes would drive a motion that is confined to the upper layer and are negligible in the bulk.

Figure 5 shows the variation of $\rho - \rho_0$ as a function of the thickness. The density is $\rho = \rho_0[1 - \hat{\alpha}(\theta^* - \theta_0^*) + \hat{\beta}(S^*$

TABLE I. The vertical component of the velocity w_i, temperature $\tilde{\theta}_i$, and salinity $\tilde{S}_i$ in the lower layer $i=1$ and the upper layer $i=2$, are discretized in the z variable with the Chebyshev-tau scheme. The expansions are of the form $\Sigma_{n=0} c_n T_n(z_i) \exp(i\alpha x)$, where z_i denote the z variables in each fluid which have been rescaled to $[-1,1]$ and given in (12). The calculation of the coefficients is described in Sec. IV B. This table lists the first five coefficients c_n for each of the variables for the eigenfunction at $\alpha=900$, $M=4$, $N=40$, $R_T = -2.9 \times 10^{10}$, $R_S = -2.5 \times 10^9$, $l_1 = 0.998\,75$, $c_E = 0.022\,85$, $\tau = 0.01$, $P=8$.

n	ω_1	ω_2	$\tilde{\theta}_1$	$\tilde{\theta}_2$	$\tilde{S}_1$	$\tilde{S}_2$
0	−0.051	−0.616	−0.47E−7	−0.50E−6	−0.49E−4	−0.47E−2
1	−0.102	0.701	−0.94E−7	0.49E−6	−0.97E−4	−0.67E−3
2	−0.101	−0.027	−0.93E−7	0.17E−7	−0.97E−4	0.74E−3
3	−0.100	−0.050	−0.91E−7	−0.60E−8	−0.96E−4	−0.13E−3
4	−0.098	−0.009	−0.89E−7	0.22E−9	−0.96E−4	−0.10E−3

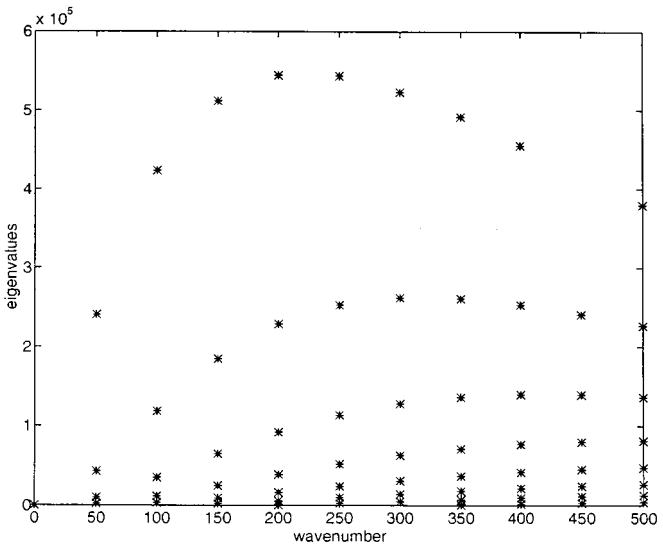

FIG. 4. The unstable eigenvalues (boundary layer modes) are plotted against wave numbers for $R_T=-2\times10^{10}$, $R_S=-10^9$, $P=8$, $\tau=0.01$, $l_2^*=5$ cm, $l_1=0.975$, $c_E=1.\dot{6}$, data given at $\alpha=0,50,...,500$.

$-S_0^*)]$, where $\rho_0=1$ gm/cm^3, $\hat{\alpha}=0.000\,22$/°C, $(\theta_0^*-\theta_1^*)/L=0.1$ °C/m, $L=2$ m, $\hat{\beta}=0.8$ units per concentration, $c_E=0.022\,85$, $S_1^*-S_0^*=-S_1^*c_E$ from Eqs. (2) and (4), $\theta_0^*=18$ °C. The base temperature field $\theta=1-z$, and salinity field (5) are used. Figure 5 shows that the density is decreasing over the lower layer, and thus stably stratified there, while increasing over the upper boundary layer. We correlate this variation with the type of instability that is described by the eigenfunctions of Figs. 2 and 3. Those eigenfunctions live in the boundary layer, where the density is destabilizing, so we conclude that those modes are analogous to the classical Bénard modes. The Bénard problem concerns motions that arise when a layer of liquid is heated from below. The

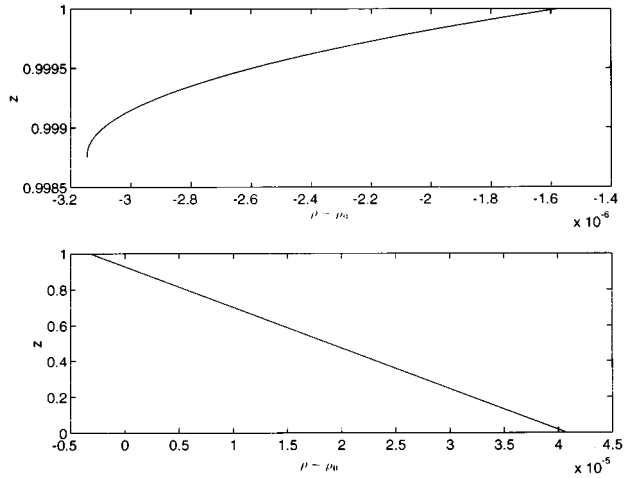

FIG. 5. The density distribution $\rho-\rho_0$ as a function of z for the situation in Figs. 2 and 3. The lower plot covers $0<z<1$, and the upper plot is a magnification close to the top surface. $\rho=1$, $l_2^*=2.5$ mm, other parameters as in Fig. 2.

double-diffusive modes, on the other hand, would take place when the density is stably stratified, and is driven by the difference in the competing diffusivities.

In summary, the extreme salinity gradient in the upper layer drives a motion that is confined to a depth of a few boundary layers. Significant motion in the lower layer was not found. The mechanism of instability that operates in the boundary layer is effectively stabilized by the temperature gradient in the bulk. However, our model is an extreme case, which has been chosen to introduce a strong up–down asymmetry; a more appropriate model is one that allows some salinity gradient in the bulk as well. This motivates the analysis of the Sec. V.

V. BOUNDARY-LAYER MODEL WITH SALINITY GRADIENT IN THE BULK

A. Governing equations

We consider the arrangement with a sharp salinity profile at the surface, above a moderate salinity gradient in the bulk [Fig. 1(b)]:

$$S=\begin{cases}1-(1-S_B)(z/l_1) & \text{for } 0<z<l_1\\ 1-(1-S_B)(z/l_1)+d_n(z-l_1)^n, & n=2,3,\ldots\end{cases}$$

$$\text{for } l_1<z<1, \qquad (15)$$

the salinity S_B at $z=l_1$ is prescribed. The boundary and $z=l_1$ conditions on S yield $d_n=[-1+(c_E-l_2)(S_B-1)/l_1]/[l_2^n(n-c_E)]$. The basic pressure field is changed from (6) but is decoupled from the calculation of the other variables. The salinity equation (8) changes to that of (9) and the rest of the equations from (7) to the end of Sec. IV A still apply. The value of the dimensionless salinity S varies from 1 at the lower boundary to $S_B<1$ at the position $z=l_1$, to a smaller value at the top. Values of S_B will be chosen in the following manner to illustrate the effect of the bulk salinity gradient. We set

$$S^*_{z=l_1}=S_1^*+\gamma, \quad S^*_{\text{top}}=S_1^*+\tilde{\gamma}\gamma, \qquad (16)$$

so that the salinity difference in the upper layer versus the salinity difference in the lower layer is in the ratio $(\tilde{\gamma}-1)$:1. This ratio is physically important and will be referred to in Sec. V B. For each $\tilde{\gamma}$ that we choose, we can calculate $\gamma=(S^*_{\text{top}}-S_1^*)/\tilde{\gamma}, S^*_{\text{top}}=S_0^*+S_{\text{top}}(S_1^*-S_0^*)$,

$$S_B=\left(\tilde{\gamma}-\frac{1}{l_1}-\frac{1+(c_E-l_2)/l_1}{n-c_E}\right)\Bigg/$$

$$\left(\tilde{\gamma}-\frac{1}{l_1}-\frac{(c_E-l_2)/l_1}{n-c_E}\right), \qquad (17)$$

where S_{top} is found from (15) with $z=1$.

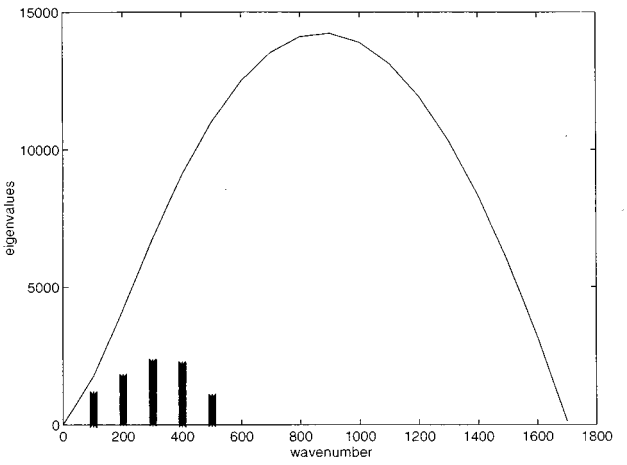

FIG. 6. Eigenvalues are plotted against wave numbers for $l_2^*=2.5$ mm, $S_B\approx 0.488$, other parameters as in Fig. 2.

B. Numerical results

We consider the quadratic profile $n=2$ in (15). The Rayleigh numbers and other conditions are the same as those of Sec. IV: $R_T=-2.9\times10^{10}$, $R_S=-2.5\times10^{9}$, $l_1=0.998\,75$, $c_E=0.022\,85$, $\tau=0.01$, $P=8$. We first set $\tilde{\gamma}=2$ to have equal salinity differences across each layer. From Eq. (17), $S_B=0.487\,979\,9$. The density variation $\rho-\rho_0$ vs z remains essentially the same as Fig. 5, with the same turn-around at approximately $z=l_1$, though the scale for the variation in the upper layer is smaller in this case. The density variation is stabilizing in the lower layer and destabilizing in the upper boundary layer.

As in the previous model with no salinity gradient in the bulk, the peak growth rate is achieved at $\alpha\approx900$. The growth rate is larger here, since the effective salinity Rayleigh number has increased with the introduction of the gradient in the bulk. Figure 6 shows the distribution of eigenvalues over the range where there is instability $0<\alpha<1800$. The results are obtained at $\alpha=0,100,...$ with $N=40$, $M=4$ in (12). The largest growth rate mode is a boundary-layer mode ($\alpha=900$, $\sigma=14\,233$). This mode is well-separated from the rest of the unstable modes. The eigenfunction for the boundary-layer mode represents motion confined to depths of a few boundary layers, and decays fast to zero in the lower layer. The rest of the unstable modes in Fig. 6 are bulk modes, over $\alpha=100$–500, peaking at $\alpha\approx300$. These are double diffusive convection rolls that extend through the lower layer. The density variation $\rho-\rho_0$ in the lower layer is stabilizing, and the instability there is driven by the competition between the solutal and thermal diffusivities. These modes can support salt fingers over the bulk of the layer.

Figures 7(a) and 7(b) illustrate that the leading bulk mode consists of a convection roll extending through the lower layer and a roll of much smaller magnitude in the upper boundary layer. Figure 7(a) shows contour plots for the vertical component of the velocity $w(x,z)$ for $0<x<2\pi/\alpha$. The upper plot shows the rolls in the boundary layer and the lower plot shows the dominant roll in the bulk of the fluid. Figure 7(b) shows the velocity component w along $x=0$, showing that the magnitude of the motion in the

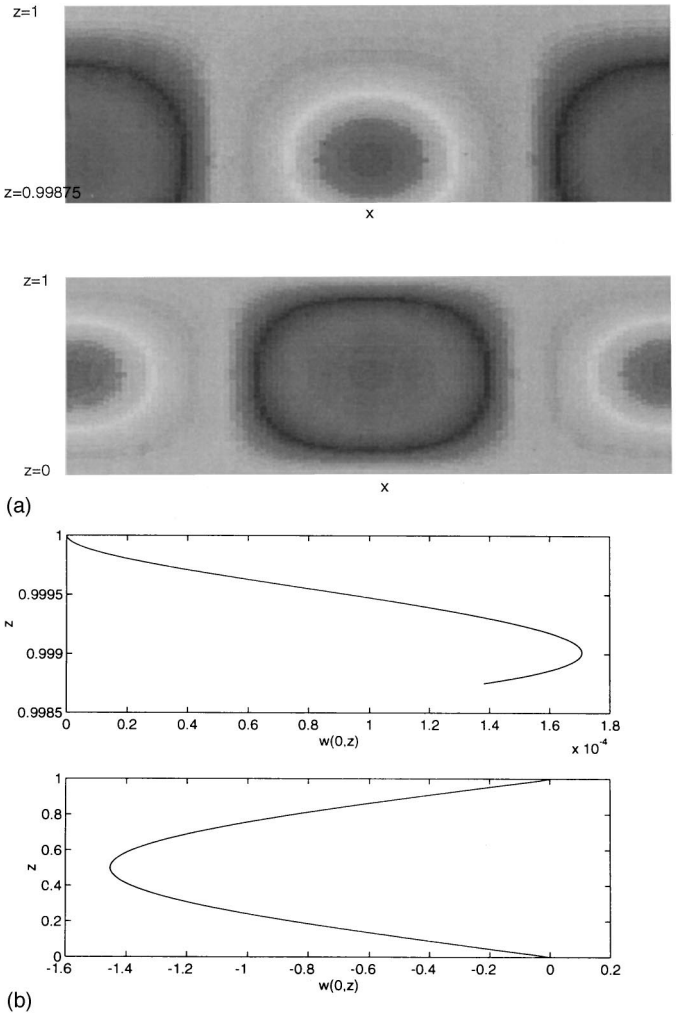

FIG. 7. (a) Contour plot for the vertical component of the velocity, in the boundary layer for the upper figure, and over the entire depth in the lower figure. The horizontal extent is one wavelength $0<x<2\pi/\alpha$. The mode is the second largest growth rate mode, the leading unstable bulk mode, for $\alpha=500$, other parameters as in Fig. 6. (b) The vertical component of the velocity versus z along the line $x=0$. The upper figure is for the boundary layer and the lower figure is for the lower layer. Contour values for (a) can be found from (b).

boundary layer is negligible compared with that of the lower layer. Since the roll in the boundary layer is negligible, this mode is up–down symmetric and is not expected on its own to drive a hexagonal solution nonlinearly near onset. However, if such a double-diffusive mode interacts with the boundary-layer modes, there is potential for asymmetric salt fingers penetrating through the bulk of the layer.

The effect of changing the relative salinities in each layer is examined by adjusting the parameter $\tilde{\gamma}$ defined in Eq. (16). If the salinity gradient in the upper layer is increased, there are a number of boundary-layer modes unstable, as also happens with a larger l_2^*. The effect of decreasing the salinity gradient in the bulk is that the double-diffusive bulk modes are stabilized. When the salinity gradient in the lower layer is steadily decreased to 0, it is found that the bulk modes stabilize and the model returns to that of Sec. IV.

The two families of modes, when having comparable

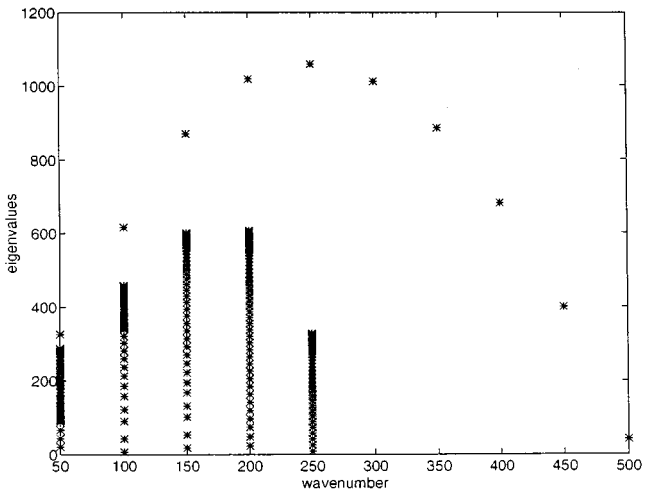

FIG. 8. The unstable eigenvalues are plotted against wave numbers for $R_T=-2\times10^9$, $R_S=-10^8$, $P=8$, $\tau=0.01$, $l_2^*=5$ mm, $l_1=0.9975$, $c_E=0.16\dot{}$, $\tilde{\gamma}=1.7$, $S_B\approx0.103$, $N=40$, $M=4$ in (12).

growth rates, may together potentially drive asymmetric salt fingers. By adjusting various parameters, such as lowering the Rayleigh numbers, increasing the salinity gradient in the bulk, and increasing the boundary-layer thickness, it is possible to arrive at situations where their growth rates are similar and the minimum achieved for a reasonable wavelength. A close example is Fig. 8 where bulk modes peak at $\alpha\approx200$ (dimensional wavelength 6 cm).

Our Rayleigh numbers are based on bulk properties, while much of the action in our model is occurring on much shorter length scales. The following trends have been found. Increasing the boundary-layer thickness while keeping the same bulk Rayleigh numbers destabilizes the boundary-layer modes. Decreasing the Rayleigh numbers while keeping other parameters fixed decreases the wave number of the largest growth rate mode to compare more favorably with the observed finger spacing described in Sec. II. By adjusting the salinity gradient distribution in the bulk and the boundary layer in the base solution, and the effective Rayleigh numbers in the boundary layer, the linear stability analysis can yield double-diffusive modes in the bulk and Bénard modes in the boundary layer with comparable but large growth rates. In this case, a study of the nonlinear interaction of these modes would be of interest. This mechanism, however, is not likely to drive the salt fingers of Ref. 6 which begin half a meter down, and we need to consider the effect of surface warming which is addressed next.

VI. A WARMED SURFACE MODEL

A. Governing equations

Osborn[6] writes that the ocean surface was ''warming daily and, at the time of the measurements, the air was 1 to 2 °C warmer than the sea surface. The air became warmer than the surface shortly after sunrise.'' The measurements were taken in the hours before noon near the surface and in the mid-afternoon for the seasonal thermocline. Concerning his Fig. 5, he writes ''The temperature-versus-depth relation of 19 April is consistent among all the profiles and can be described as three regions. Region I is a layer with a strong near-surface gradient (~1 m thick); region II is a quasi-isothermal layer (~3 m thick); and region III has a steadily decreasing temperature.'' There is a near-surface turbulent region of about 0.5 m deep; the plumes begin below this and extend to about 3 m in quiescent water. They disappear in the top of region III. We model this temperature profile with three layers occupying $0<z^*<L$ [Fig. 1(c)]. The three layers have thicknesses $L-d_2^*$, $d_2^*-d_1^*$, and d_1^* cm. Regions III, II, and I denote $0<z^*<d_1^*$, $d_1^*<z^*<d_2^*$ and $d_2^*<z^*<L$, respectively, or in dimensionless variables, $0<z<d_1$, $d_1<z<d_2$, and $d_2<z<1$. The temperature at the surface $z^*=L$ is θ_0^*, at $z^*=d_2^*$ it is θ_3^*, at $z^*=d_1^*$ it is θ_2^*, at the bottom $z^*=0$ it is θ_1^*, and $\theta_0^*>\theta_3^*>\theta_2^*>\theta_1^*$.

The temperature profile is steep in the shallow region I, almost constant in the larger region II, and then varies moderately in a deep region III. This profile does not possess up–down symmetry and is thus a candidate for asymmetric salt fingers. The competition between this nonlinear stabilizing temperature profile and a linear destabilizing salinity gradient $S=1-z$, will be examined. The temperature gradient can stabilize salt fingers in the top and bottom layers, while the salinity gradient destabilizes them in the middle layer.

The sharp temperature gradient in region I is due to warming from solar radiation and we model this by introducing a source term which is a function of z, into the right-hand side of the heat equation (see the first paragraph of Sec. III). This would lead to exponential decay but as a first attempt to account for this, we apply a quadratic variation to simplify the analysis. In the other layers, we also use a polynomial variation with z: linear in region II and quadratic in region III. The data show gradients in regions II and III to be close to linear, with almost a discontinuity in slope. The boundary conditions are: $\theta=0$ at $z=1$ (top), $\theta=1$ at $z=0$ (bottom), $\theta=\theta_2$ at $z=d_1$, $\theta=\theta_3$, at $z=d_2$, and $[\![\partial\theta/\partial z]\!]=0$ at $z=d_1,d_2$ (continuity of heat flux). Our basic temperature profile is

$$\theta=\begin{cases}1+A_1z^2+A_2z & \text{for } 0<z<d_1\\ A_3(z-d_1)+\theta_2 & \text{for } d_1<z<d_2\\ A_4(z-1)^2+A_5(z-1) & \text{for } d_2<z<1,\end{cases} \tag{18}$$

$$A_1=\frac{1-\theta_2}{d_1^2}+\frac{(\theta_3-\theta_2)}{d_1(d_2-d_1)},$$

$$A_2=-\frac{\theta_3-\theta_2}{d_2-d_1}-\frac{2(1-\theta_2)}{d_1},$$

$$A_3=\frac{\theta_3-\theta_2}{d_2-d_1},\quad A_4=\frac{-\theta_3}{(d_2-1)^2}+\frac{\theta_3-\theta_2}{(d_2-1)(d_2-d_1)},$$

$$A_5=\frac{(\theta_2-\theta_3)}{d_2-d_1}+\frac{2\theta_3}{d_2-1}.$$

The perturbations $u,w,\tilde{\theta},\tilde{p},\tilde{S}$ satisfy the momentum and incompressibility equations, $\tilde{\theta}+w(\partial\theta/\partial z)-\Delta\tilde{\theta}=-(\mathbf{v}\cdot\nabla)\tilde{\theta}$, and $\tilde{S}-w-\tau\Delta\tilde{S}=-(\mathbf{v}\cdot\nabla)\tilde{S}$, where $\partial\theta/\partial z$ is found from (18). The perturbation temperature satisfies $\tilde{\theta}=0$ at $z=0,1$. To be consistent with the base salinity, the top condition is $\tilde{S}=0$ at $z=1$, and the bottom condition is (11). The top and bottom boundaries are modeled as stress-free surfaces since the salt-finger phenomena occur in a layer within the ocean, sand-

wiched between fluid layers. At $z=d_1,d_2$, we have the continuity conditions listed at the end of Sec. IV A.

B. Numerical results on linear stability

We use incompressibility to eliminate u in favor of w, and use the x component of the momentum equation to eliminate p. We discretize $\tilde{\theta},\tilde{S},w$ using Chebyshev polynomials of degree 0 to N_1 in region I, to N_2 in region II, to N_3 in region III; for example, $\tilde{\theta} = \exp(i\alpha x + \sigma t)\Sigma_{n=0}^{N_1} t_n T_n(z_1)$ in region I. The z_i are $2(z-d_1)/d_1+1$ for $i=3$ (region III), $2(z-d_2)/(d_2-d_1)+1$ for $i=2$ (region II), $2(z-1)/(1-d_2)+1$ for $i=1$ (region I). The z_i cover the interval $[-1,1]$ in each layer. This results in $3(N_i+1)$ unknown coefficients in layer i, a total of $3(N_1+N_2+N_3+3)$ unknowns. The appropriate values for N_i are found through convergence tests. As in Sec. IV B, the momentum equation is discretized and truncated beyond the (N_i-4)th Chebyshev mode in layer i, yielding N_i-3 equations, and the solute and heat transport equations are truncated beyond the (N_i-2)th degree in layer i, yielding N_i-1 equations each. This results in $3(N_1+N_1+N_3)-15$ equations. The conditions at $z=d_i$ are the continuity of $\tilde{\theta}$, $d\tilde{\theta}/dz$, $\tilde{S}$, $d\tilde{S}/dz$, w, w_z, w_{zz}, and w_{zzz}. At the top and bottom boundaries, $\tilde{\theta},w,w_{zz}$ vanish, and $\tilde{S}=0$ at the top and the bottom. Altogether, there are 24 conditions. This results in a $3(N_1+N_2+N_3)+9$ matrix eigenvalue problem.

In the long-wave limit $\alpha\to 0$, incompressibility $i\alpha u+w_z=0$ implies that $w_z=0$. The boundary conditions are $w=0$ at $z=0,1$, so that w is identically 0. This reduces the eigenvalue problem to three Sturm–Liouville systems, decoupling the problems for temperature, salinity, and u: $\sigma\tilde{\theta}-\tilde{\theta}_{zz}=0$, $\tilde{\theta}=0$ at $z=0,1$ $\sigma\tilde{S}-\tau\tilde{S}_{zz}=0$, $\tilde{S}=0$ at $z=0,1$, and $\sigma\psi_{zz}-P\psi_{zzzz}=0$, $\psi=\psi_{zz}=0$ at $z=0,1$, where ψ denotes the streamfunction with $u=\psi_z$. We find $\tilde{\theta}=\sinh\sqrt{\sigma}z$, $\tilde{S}=\sinh\sqrt{\sigma/\tau}z$, $u=\cosh\sqrt{\sigma/P}z$, $\sigma=-n^2\pi^2,-n^2\pi^2\tau,-n^2\pi^2P,n=1,2,...$ This was checked with the code.

We refer to the temperature and salinity profiles of Fig. 5 of Ref. 6 for the numerical values of parameters: $\theta_0^*=18.5$ °C, $\theta_3^*=16.5$ °C, $\theta_2^*=16.3$ °C, $\theta_1^*=15.9$ °C, regions I, II, and III have thicknesses 1, 3, and 2.5 m, respectively. Thus, $L=650$ cm, the other parameters are given under Fig. 9, $\hat{\alpha}=1.5\times10^{-4}$, $\kappa_T\nu=10^{-5}$, $R_T=-10^{13}$. Since R_ρ varies over 10–20, we choose $R_S=-5\times10^{11}$ [and $\hat{\beta}(S_1^*-S_0^*)=-0.000\,018$]. Figure 9 shows the temperature $\theta^*=\theta(\theta_1^*-\theta_0^*)+\theta_0^*$, and this is similar to Fig. 5 of Ref. 6. Figure 10 shows the depth z versus the density variation $\rho-1=0.000\,39\theta-0.000\,018S$, where θ is given in (18) and $S=1-z$. This shows that the density profile is stabilizing and an instability would be due to diffusive effects rather than the Bénard-type of instability.

In order to visualize the eigenfunctions of largest growth rates, we switch to lower Rayleigh numbers. Numerical results show that the mode which first becomes unstable at lower R_S remains the most unstable mode at higher values. The structure of the mode remains qualitatively the same in the large-R_T range. Figure 11 shows the structure of the vertical component of the velocity w of the eigenfunction for the most unstable mode at $R_T=-2\times10^9$, $R_S=-3.5\times10^6$ $(N_1=N_2=N_3=25)$. The upper part of Fig. 11 shows the contours for w. The horizontal coordinate is x, over one wavelength $0\leqslant x\leqslant 2\pi/\alpha$, and the vertical coordinate is z, $0\leqslant z\leqslant 1$. There is one cell extending over the depth of region II. The lower graph shows w along $x=0$, versus z for $0\leqslant z\leqslant 1$. There is upflow along $x=0$ and downflow at $x=$half wavelength. It is clear from Fig. 11 that there is double-diffusive instability in region II, extending out of the bottom of region I and ending at the top of region III. The eigenfunction for the second largest growth rate has two cells extending over the depth of region II, and so on for the higher modes. Osborn writes ''we cannot tell if individual plumes extend down that entire distance,'' and since the growth rates of these modes are comparable, it is not possible to state from this analysis which ones are preferred.

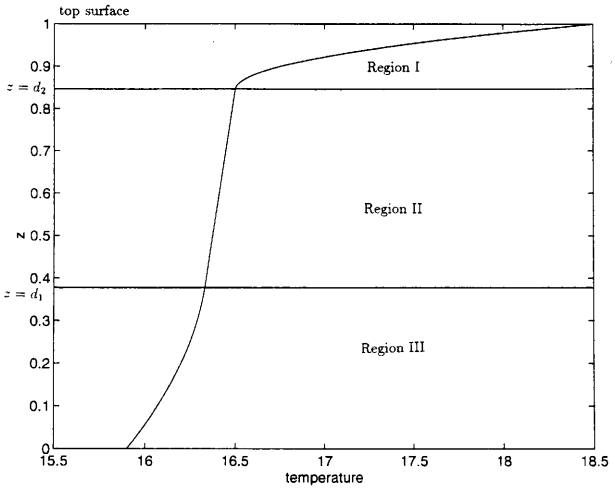

FIG. 9. The dimensional temperature θ^* vs the depth variable z, $d_1\approx0.39$, $d_2\approx0.85$, $\theta_2\approx0.83$, $\theta_3\approx0.77$, $A_1\approx0.77$, $A_2\approx-.73$, $A_3\approx-0.14$, $A_4\approx-31.6$, $A_5\approx-9.86$.

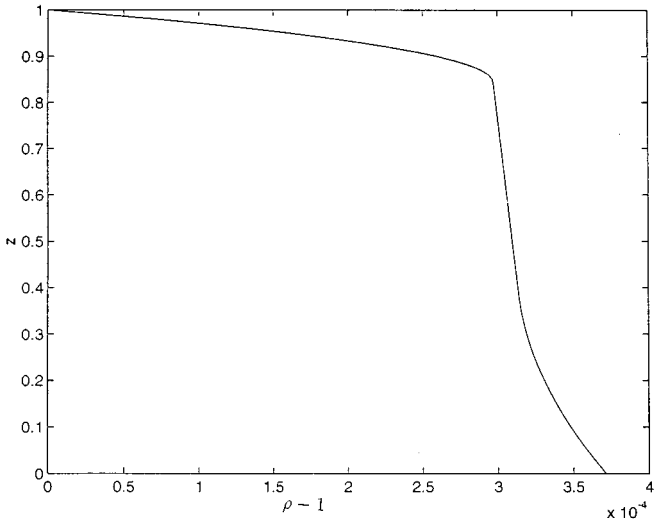

FIG. 10. The density variation $\rho-\rho_0$ where $\rho_0=1$ in cgs units vs the depth variable z for $0\leqslant z\leqslant 1$. $R_T=-1.0e+13$, $R_S=-5.0e+11$. The temperature profile is that of Fig. 9.

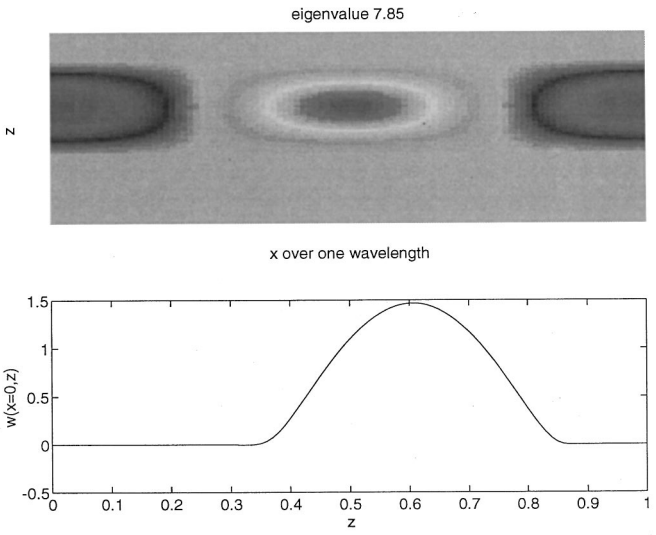

FIG. 11. Upper: a contour plot of the vertical component of velocity w for the eigenfunction of largest growth rate $\sigma=7.853$, $\alpha=70$, $R_T=-2\times10^9$, $R_S=-3.5\times10^6$, $P=8$, $\tau=0.01$. The horizontal extent is one wavelength $0<x<2\pi/\alpha$, and the vertical extent is $0<z<1$. The cell extends through $d_1<z<d_2$. Lower: $w(x,z)$ at $x=0$, vs z, showing upflow. The downflow occurs at $x=$half wavelength. Contour values for the upper graph can be found from the lower graph.

However, the unstable modes are reminiscent of salt fingers that begin at the bottom of region I and end at the top of region III.

The trend as the Rayleigh numbers are increased is that many modes become unstable at a given wave number and are close to each other, the largest growth rates occur at higher wave numbers. Growth rates over an ever wider range of wave numbers are comparable. This is illustrated in Fig. 12, which shows the eigenvalue distribution at $R_T=-10^{13}$, $R_S=-5\times10^{11}$ ($N_1=N_2=N_3=30$). At $\alpha=100$, the growth rate is already of order 10^4 and at $\alpha=1200$, the largest eigenvalue is still 0.2×10^6. The maximum growth rate is achieved for $\alpha\approx1000$, which yields a dimensional wavelength of 4 cm, close to the Q spacing of the observed salt fingers (see discussion at the end of Sec. II). The distribution of the eigenvalues is similar to that of the classical double diffusion problem at high Rayleigh numbers. Due to the number and close proximity of the unstable eigenvalues, it is not possible to conclude from the linear stability analysis what the nonlinear solution would be. The mechanism of surface warming, however, yields the type of vertical structure as described in Ref. 6. The up–down asymmetry in the linear two-dimensional analysis is a promising mechanism for a hexagonal pattern in three-dimensions. A weakly nonlinear study of the onset of instability is planned for future work in order to test whether the hexagonal pattern would be preferred. To check the relevance of the theory, some careful experiments are needed.

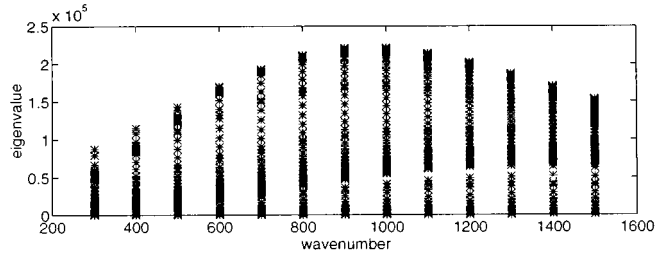

FIG. 12. The unstable eigenvalues at $\alpha=300$–1500 for $R_T=-10^{13}$, $R_S=-5\times10^{11}$, $P=8$, $\tau=0.01$ for the temperature and density profiles of Figs. 9 and 10. $N_1=N_2=N_3=30$ Chebyshev modes are used.

VII. CONCLUSION

We have examined the linear stability of three models: the salty boundary-layer model, the boundary layer model modified by a weak salinity gradient in the bulk, and the warmed surface model. The first two concern the mechanism of surface evaporation, and the third concerns heating due to solar radiation.

The salty boundary-layer model possesses a long-wave instability. At higher Rayleigh numbers, the largest growth rates are driven by a destabilizing density gradient, as in the case of Bénard convection. These modes extend to depths of the order of the boundary-layer thickness and are dissipated by the stabilizing temperature gradient in the bulk. The modified model with weak salinity gradient in the bulk has the boundary-layer modes as well as bulk double-diffusive modes driven by the diffusivities in the presence of a stabilizing density profile. These modes may interact nonlinearly to drive salt fingers that extend through the bulk.

The warmed surface model has a steep temperature gradient at the top, gentle in the middle, and moderate gradient below. In contrast to the earlier cases, this model has a finite critical wave number, and a weakly nonlinear analysis can be treated with the method of Ref. 12. The critical eigenfunctions, as well as the largest growth rate modes at higher Rayleigh numbers, represent salt fingers that extend through the middle layer. For the oceanic parameters, there are many unstable modes and a weakly nonlinear analysis may not be the appropriate one for describing a selection mechanism. Other effects such as turbulence may be important. However, the vertical structure of the modes in the warmed surface model is reminiscent of the asymmetric ''salt fountains'' reported by Osborn.[6] An investigation of the horizontal structure of the preferred mode as well as the competition between rolls and hexagonal patterns will be addressed in future work. Ultimately, we must learn to understand and predict such phenomena in order to quantify their impact on the structure of the near surface warm layer, which are important in sound propagation, air–sea exchange, and upper ocean dynamics.

ACKNOWLEDGMENTS

We thank Melvin Stern for discussions. The work of Y.R. was sponsored by the ONR under Grant No. N00014-92-J-1664 and the NSF under Grant No. CTS-9307238. The work of R.S. is sponsored by the Ocean, Atmosphere and Space Division of ONR under Grant No. N00014-92-J-1323. Part of this work was carried out when Y.R. was at the Isaac Newton Institute for Mathematical Sciences, while a Visiting Fellow at Clare Hall, Cambridge, U.K.

[1]J. S. Turner, *Buoyancy Effects in Fluids* (Cambridge University Press, Cambridge, 1979).
[2]R. W. Schmitt, ''Double diffusion in oceanography,'' Annu. Rev. Fluid Mech. **26**, 255 (1994).
[3]A. J. Williams III, ''Images of ocean microstructure,'' Deep-Sea Res. **22**, 811 (1975).
[4]B. Magnell, ''Salt fingers observed in the Mediterranean outflow region (34 °N, 11 °W) using a towed sensor,'' J. Phys. Oceanogr. **6**, 511 (1976).
[5]R. B. Lambert and W. E. Sturges, ''A thermohaline staircase and vertical mixing in the thermocline,'' Deep-Sea Res. **24**, 211 (1977).
[6]T. Osborn, ''Observations of the salt fountain,'' Atmos. Ocean **29**, 340 (1991).
[7]R. W. Schmitt, ''Triangular and asymmetric salt fingers,'' J. Phys. Oceanogr. **24**, 855 (1994).
[8]L. Stramma, P. Cornillon, R. A. Weller, J. F. Price, and M. G. Bricoe, ''Large diurnal sea surface temperature variability: Satellite and *in situ* measurements,'' J. Phys. Oceanogr. **16**, 827 (1986).
[9]J. F. Price, R. A. Weller, and R. Pinkel, ''Diurnal cycling: Observations and models of the upper ocean response to diurnal heating, cooling and wind mixing,'' J. Geophys. Res. **91**, 8411 (1986).
[10]M. R. E. Proctor and J. Y. Holyer, ''Planform selection in salt fingers,'' J. Fluid Mech. **168**, 241 (1986).
[11]M. Golubitsky, J. W. Swift, and E. Knobloch, ''Symmetries and pattern selection in Rayleigh-Benard convection,'' Physica D **10**, 249 (1984).
[12]E. Buzano and M. Golubitsky, ''Bifurcation on the hexagonal lattice and the planar Benard problem,'' Philos. Trans. R. Soc. London, Ser. A **308**, 617 (1983).
[13]E. Knobloch, in *Proceedings of the 1985 Joint ASCE-ASME Mechanics Conference*, edited by N. E. Bixler and E. A. Spiegel (ASME, New York, 1985), Vol. 24, pp. 17–22.
[14]A. E. Deane, E. Knobloch, and J. Toomre, ''Traveling waves and chaos in thermosolutal convection,'' Phys. Rev. A **36**, 2862 (1987).
[15]E. Knobloch, A. E. Deane, J. Toomre, and D. R. Moore, ''Doubly diffusive waves,'' Contemp. Math. **56**, 203 (1986).
[16]W. Nagata and J. Thomas, ''Bifurcation in double-diffusive systems I. Equilibrium solutions, II. Time periodic solutions,'' SIAM J. Math. Anal. **17**, 91 (1984); ''III. Interaction of equilibrium and time periodic solutions,'' *ibid*. **17**, 289 (1984).
[17]P. G. Baines and A. E. Gill, ''On thermohaline convection with linear gradients,'' J. Fluid Mech. **37**, 289 (1969).
[18]Y. Y. Renardy, ''Pattern selection for the oscillatory onset in thermosolutal convection,'' Phys. Fluids A **5**, 1376 (1993).
[19]R. W. Schmitt, ''The growth rate of super-critical salt fingers,'' Deep-Sea Res. **26**, 23 (1979).
[20]A. Schluter, D. Lortz, and F. H. Busse, ''On the stability of steady finite amplitude convection,'' J. Fluid Mech. **23**, 129 (1965).
[21]M. Renardy and Y. Renardy, ''Pattern selection in the Bénard problem for a viscoelastic fluid,'' Z. Angew. Math. Phys. **43**, 154 (1992).
[22]R. Krishnamurti, ''Finite amplitude convection with changing mean temperature,'' J. Fluid Mech. **33**, 445 (1968).
[23]M. Stern, *Ocean Circulation Physics* (Academic, New York, 1975).
[24]D. Gottlieb and S. A. Orszag, *Numerical Analysis of Spectral Methods: Theory and Applications*, CBMS-NSF Regional Conference Series in Applied Math. (SIAM, Philadelphia, 1983).
[25]D. D. Joseph and Y. Y. Renardy, *Fundamentals of Two-Fluid Dynamics, Parts 1 and 2* (Springer Verlag, New York, 1993).
[26]Y. Renardy, ''Planforms at the onset of instability in double diffusive convection,'' Naval Res. Rev. **47**(1), 29 (1995).
[27]K. Fujimura and Y. Renardy, ''The 2:1 steady-Hopf mode interaction in the two-layer Bénard problem,'' Physica D **85**, 25 (1995).